Article type: Full Article

Title: Assessment of tissue polarimetric properties using Stokes polarimetric imaging with circularly polarized illumination

Ji Qi [1,2, +], Honghui He [4,5,+], Jianyu Lin[,1,2], Yang Dong[4,5], Dongsheng Chen[4,5], Hui Ma[3,4,5] *, Daniel S. Elson[1,2,] *

[+]Ji Qi and Honghui He have made an equal contribution to this paper

*Corresponding Author: E-mail: (daniel.elson@imperial.ac.uk, mahui@tsinghua.edu.cn)

[1] Hamlyn Centre for Robotic Surgery, Institute of Global Health Innovation, Imperial College London, Exhibition Road, London, SW7 2AZ, UK
[2] Department of Surgery and Cancer, Imperial College London, Exhibition Road, London, SW7 2AZ, UK
[3] Center for Precision Medicine and Healthcare, Tsinghua-Berkeley Shenzhen Institute, Shenzhen 518071, China
[4]Shenzhen Key Laboratory for Minimal Invasive Medical Technologies, Institute of Optical Imaging and Sensing, Graduate School at Shenzhen, Tsinghua University, Shenzhen, 518005, China
[5]Department of Physics, Tsinghua University, Beijing, 100084, China

Short title: J. Qi et al.: Short title (Assessment of tissue polarimetric properties using Stokes polarimetric imaging)

Abstract Tissue depolarization and linear retardance are the main polarization characteristics of interest for bulk tissue characterization, and are normally interpreted from Mueller polarimetry. Stokes polarimetry can be conducted using simpler instrumentation and in a shorter time. Here we use Stokes polarimetric imaging with circularly polarized illumination to assess the circular depolarization and linear retardance properties of tissue. Results obtained were compared with Mueller polarimetry in transmission and reflection geometry respectively. It is found that circular depolarization obtained from these two methods is very similar in both geometries, and that linear retardance is highly quantitatively similar for transmission geometry and qualitatively similar for reflection geometry. The majority of tissue circular depolarization and linear retardance image information (represented by local image contrast features) obtained from Mueller polarimetry is well preserved from Stokes polarimetry in both geometries. These findings can be referred to for further understanding tissue Stokes polarimetric data, and for further application of Stokes

polarimetry under the circumstances where short acquisition time or low optical system complexity is a priority, such as polarimetric endoscopy and microscopy.

1. Introduction

The primary polarization properties of a sample are the depolarization, retardance – including linear and circular retardance - and diattenuation[1, 2]. These properties – especially depolarization and linear retardance – have been used to investigate biological tissue microstructure and composition and could benefit tissue diagnosis and image guided therapy [3-6]. It has been reported that tissue linear retardance contributes to partial bladder obstruction assessment [7], non-staining microscopy for liver fibrosis and cervical cancer diagnosis [8-10], characterization of RF ablation extent in myocardium [11, 12] etc. It has also been demonstrated that tissue depolarization is able to quickly identify the stage of colon cancer development [13-15], to assess residual cancerous tissue after radio-chemical therapy [16], to diagnose oesophageal cancer [17] and to enhance image contrast of tissue textures [3, 5, 18]. Mueller matrices give a comprehensive characterization of tissue polarization properties after interpretation methods have been applied [1, 19-24]. With advances in the past decades, Mueller polarimetry has demonstrated great potential in tissue diagnosis [25]. Many findings like those mentioned in the first paragraph were made based on tissue Mueller polarimetry. Complete Mueller polarimetric imaging involves time-sequential image acquisition (normally at least 16 radiometric images) and normally requires relatively long acquisition time, which makes it challenging to image moving or deforming objects. The Mueller imaging polarimeter also requires a pair of active polarization state modulators based on mechanical devices, liquid crystal variable retarders, or photo-elastic modulators, etc. as polarization state generators (PSG) and analyzers (PSA) respectively, which may become a problem in terms of technical difficulty and economic cost in some settings, e.g. Mueller polarimetric endoscopy which requires miniaturization and real-time operation, as well as microscopy for *in vivo* medical and biology studies that involves moving objects.

Stokes polarimetry only requires measurement of the polarization state of the emergent light from samples. Stokes polarimetry can ease instrumentation and makes it feasible to do real-time polarimetric imaging [26] (compared with complete Mueller polarimetry and 3×3 Mueller polarimetry). Note that there has been a number of snapshot Stokes polarimetric imaging designs [27]. Stokes polarimetry (including partial Stokes polarimetry) has been shown to be useful for atmospheric remote sensing [28], target recognition [27], and astronomical observation [29]. With the polarization state of the illumination light predetermined (i.e. no active PSG), Stokes polarimetry also demonstrated potential for biomedical applications. Wu *et al.* demonstrated that Stokes polarimetric imaging together with rotating linearly polarized [30] or circularly polarized illumination [31] can be used to reveal subsurface tissue structural information that could be useful for diagnosis. Macdonald *et al.* reported that optical clearing in turbid media can be observed and quantitatively analysed with Stokes polarimetry [32], in which circularly polarised light was employed due to its strong polarization memory in Mie-sized scattered dominates turbid media. Kunnen *et al.* employed Stokes polarimetric detection with circularly and elliptically polarized light for cancerous tissue identification [33]. It is noted that the tissue Stokes polarimetric data acquired in the work mentioned above were analysed with different methodologies, and were not analysed in terms of the primary polarization properties as is normally done in tissue Mueller polarimetry.

As reviewed in the first paragraph, tissue Mueller polarimetric studies indicate that depolarization and linear retardance are found to be the main polarization characteristics of interest and usefulness, and the magnitude of diattenuation for the majority of tissue types is typically very

small [34-36], with only a small number of exceptions like skeletal muscle and heart muscle [24]. Here, we use Stokes polarimetry with circularly polarized illumination to approximate two tissue polarization properties of interest which are normally obtained from tissue Mueller polarimetry - circular depolarization and the magnitude of linear retardance for several biological tissues. The findings can be referred to for further understanding tissue Stokes polarimetric data, and for further application of Stokes polarimetry under the circumstances where Mueller polarimetric imaging is difficult to implement, such as polarimetric endoscopy.

2. Methods

2.1 Setup

Three setups have been used to partly explore the generalisability of the proposed Stokes polarimetry method. Setup 1 is an imaging polarimeter constructed in the dual-rotating-quarter-waveplate configuration, as displayed in Fig. 1. A red LED (centre wavelength 633 nm, 15 nm bandwidth, 3 W, CREE, xlamp XP-E R2) together with a pinhole and a collimating lens (f= 60 mm) provided approximately collimated illumination (diameter 18 mm). The polarization state generator (PSG) and polarization state analyzer (PSA) consisted of a fixed linear polarizer and a rotatable quarter waveplate and the detection arm included an imaging lens (f= 100 mm) and a CCD (QImaging 32-0122A, Canada). When the polarimeter was operated in a Mueller polarimetric mode, the waveplates in the PSG and PSA denoted by QW1 and QW2 respectively were rotated in an angular speed ratio of 1:5 with QW1 rotated from 0° to 180° in steps of 6°. The polarimeter was then calibrated according to [37]. When the polarimeter was used in a Stokes polarimetric mode, the PSG waveplate remained stationary while the PSA waveplate was rotated in a step of 15° from 0° to 180°. The input polarization state in the Stokes polarimetric mode was made to be as circular as possible and was measured to be [1 0.0185 0.0011 0.9998]. The polarimeter can be used for both transmission (Fig. 1(a)) and reflection (Fig. 1(b)) measurements. In reflection geometry, the optical axis of the detection arm was oriented at 20° with respect to the illumination arm. Setup 2 is the microscope version of Setup 1 in transmission mode, and was based on the same type of light source, PSG and PSA and calibration method as Setup 1. More technical details of this Mueller polarimetric microscope can be found in [10]. Mueller measurements were conducted in accordance to Setup 1. Setup 3 is another imaging Mueller polarimeter consisting of a narrow band light source (546 nm centre wavelength/20 nm bandwidth), a PSG (a fixed 0° linear polarizer and a rotating quarter waveplate rotated to -45°, 0°, 30°, 60°) and a PSA which is a motorized filter wheel containing four linear polarizers (0°, 45°, 90°, 135°) and two circular polarizers (left and right). The setup was calibrated based on Eigenvalue calibration method [38]. The Stokes measurements for Setups 2 and 3 were calculated based on the Mueller matrix images acquired multiplying the incident Stokes vector $[1\ 0.0185\ 0.0011\ 0.9998]^T$ (the superscripted T refers to transposed) so as to keep consistent with the results obtained using Setup 1. Since this study mainly focused on the comparison of the results obtained from Mueller and Stokes methods, a snapshot Stokes polarimetric imaging device was not used although there are many designs available[27]. Typical acquisition time for Mueller and Stokes polarimetric imaging for Setup 1 were about 60 seconds and 20 seconds respectively. Typical acquisition time for Mueller polarimetric imaging for Setup 2 and Setup 3 were about 60 seconds and 30 seconds respectively.
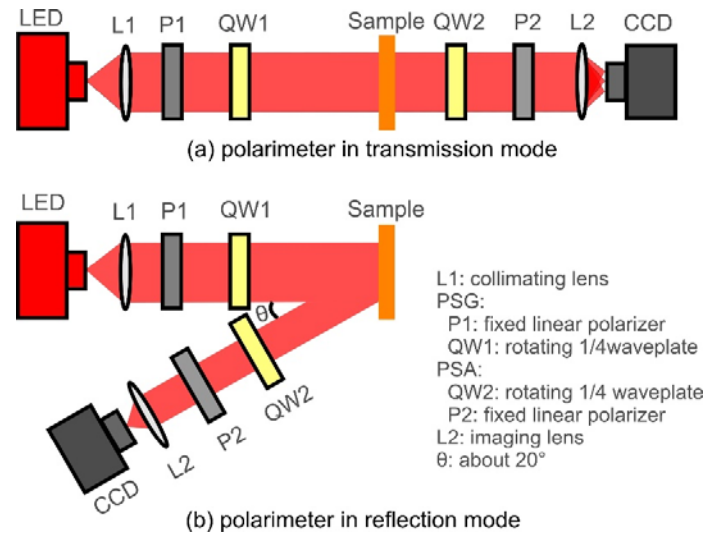
Figure 1 Experimental Setup 1 for polarimetric imaging in transmission mode (a) and reflection mode (b). When the polarimeter was used for Mueller polarimetric imaging, QW1 and QW2 respectively were rotated in an angular speed ratio of 1:5. When the polarimeter was used for Stokes polarimetric imaging, QW1 remained stationary and the QW2 was rotated.

2.2 Interpreting circular depolarization and linear retardance from polarimetric images

2.2.1 Interpretation from Stokes polarimetry with circularly polarized illumination

(*a*) *Preference of circular polarization to linear polarization for illumination*

It is proposed in this paper to use circularly polarized illumination for Stokes polarimetric imaging. Many tissue types are known to be spatially anisotropic, e.g. due to the presence of linear retardance, and there exists an anisotropy axis (e.g. fast axis) with a spatial orientation which is invisible to standard image sensors or human eyes. Linear and elliptical polarizations also have an orientation. If linearly/elliptically polarized illumination was used for Stokes polarimetric imaging, it would be impractical to keep the angle between the polarization orientation and the invisible anisotropy axis of tissue consistent among intra- and inter- sample measurements as summarized in [25]. The obvious advantage of circular polarization is that it does not have a spatial orientation, and is not sensitive to the orientation of the sample with respect to the polarimetric devices. Therefore, circularly polarized illumination was used for Stokes polarimetric imaging.

(*b*) *Circular Depolarization*

Circular depolarization generally refers to a loss of coherence of phase or amplitude of incident circularly polarized light, but there is not a standard mathematical definition [39, 40]. Experimentally quantifying depolarization could be done based on interpretation of the Mueller matrix e.g. depolarization index [41], average degree of polarization [42], depolarization entropy [43], and several decomposition based methods [1, 20, 44, 45]. Depolarization can also be achieved based on analysis of degree of polarization derived via Stokes polarimetry [46, 47] (which is used in this work) and partial Stokes polarimetric measurements [48-50]. Mathematical definitions of depolarization in these methods are not completely the same, but all stem from the physical concept of "depolarization". These definitions are not expected to give the same quantitative value, but they convey the same/similar information (e.g. local image contrast features) about depolarization.

Given that fully circularly polarized light is used for illumination, assessment of circular depolarization from Stokes vectors of scattered light by tissue becomes straightforward. Circular depolarization manifests from the reduction of the degree of polarization (*DOP*, mathematical definition shown in Eq. 1). Here the circular depolarization coefficient *dep_c-S* is defined as one

minus the ratio of *DOP*s of the incident fully circular polarized light and emergent partially polarized light, denoted by $DOP_{in}|_{cp}$ and $DOP_{out}|_{cp}$ respectively in Eq. 4. Since the incident light for Stokes polarimetric imaging is fully circularly polarized with the $DOP_{in}|_{cp}$ equal to 1. The *dep$_{c-S}$* was only determined by the $DOP_{out}|_{cp}$ which can be easily derived via measuring the emergent Stokes vector

$$dep_{c-S} = 1 - \frac{DOP_{out}|_{cp}}{DOP_{in}|_{cp}} = 1 - DOP_{out}|_{cp} \tag{1}$$

in which the *DOP* can be calculated from four Stokes parameters $[S_0, S_1, S_2, S_3]$.

$$DOP = \frac{\sqrt{S_1^2 + S_2^2 + S_3^2}}{S_0} \tag{2}$$

The circular depolarization coefficient *dep$_{c-S}$* obtained here is referred to as Stokes-depolarization in this paper, and is a dimensionless quantity with minimum value 0 (non-depolarized) and maximum value 1 (fully depolarized).
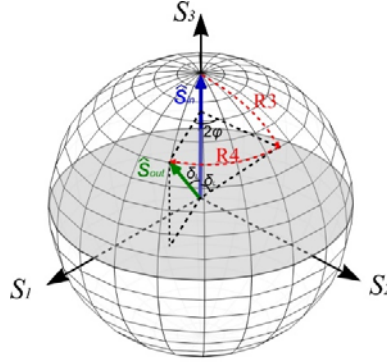
(*c*). *Linear retardance*

Figure 2. Retardance may convert the input circularly polarized light to output elliptically/linearly polarized light. The sphere in the figure is the Poincare sphere. The input polarization state ŝ$_{in}$ and the output polarization vector ŝ$_{out}$ are represented by the blue and green arrows respectively. The transformation induced by retardance characterized by R3 in Eq. (6) rotated ŝ$_{in}$ of the angle δ_L along S_2-S_3, followed by a rotation of 2φ with respect to S_3 axis characterized by R4. The angle between ŝ$_{in}$ and ŝ$_{out}$ is the magnitude of linear retardance δ_L.

Linear retardance may convert part of the circularly polarized incident light to linearly polarized light (resulting in elliptical/linear polarization). Diattenuation may also be able to convert the circularly polarized into linearly polarized light. Since tissue diattenuation is normally very small as stated in the Introduction, tissue linear retardance becomes the dominant source of linearly polarized components in the emergent light, provided that fully circularly polarized light is used for illumination. Linear retardance can then be obtained from how much linear polarized light emerges from the sample. In detail, retardance represents a rotational transformation of vectors $\hat{s}$ (which consists of the last three Stokes vector elements S_1, S_2, S_3) in the Poincare sphere [1, 51].A general retardance matrix is known as [2, 25, 52],

$$M_R = M_{LR}M_{CR}$$

$$= \begin{bmatrix} 1 & 0 & 0 & 0 \\ 0 & \cos 2\varphi & -\sin 2\varphi & 0 \\ 0 & \sin 2\varphi & \cos 2\varphi & 0 \\ 0 & 0 & 0 & 1 \end{bmatrix} \begin{bmatrix} 1 & 0 & 0 & 0 \\ 0 & 1 & 0 & 0 \\ 0 & 0 & \cos \delta_L & \sin \delta_L \\ 0 & 0 & -\sin \delta_L & \cos \delta_L \end{bmatrix} \begin{bmatrix} 1 & 0 & 0 & 0 \\ 0 & \cos 2\varphi & \sin 2\varphi & 0 \\ 0 & -\sin 2\varphi & \cos 2\varphi & 0 \\ 0 & 0 & 0 & 1 \end{bmatrix} \begin{bmatrix} 1 & 0 & 0 & 0 \\ 0 & \cos \delta_c & \sin \delta_c & 0 \\ 0 & -\sin \delta_c & \cos \delta_c & 0 \\ 0 & 0 & 0 & 1 \end{bmatrix} \tag{3}$$

where M_{LR} and M_{CR} are the linear retardance matrix and the circular retardance matrix, and the parameters δ_L, δ_C and φ are magnitudes of linear and circular retardance and linear retardance orientation (fast axis orientation) respectively. The three-dimensional rotation represented by a

general retardance matrix can break down into four consecutive two dimensional rotations named R1, R2, R3 and R4, denoted by the matrices from right to left in Eq. 6. Considering the incident light to be fully circularly polarized and represented by a Stokes vector $[1\ 0\ 0\ 1]^T$ (the superscript ^{T} refers to transposed), R1 and R2 cannot change the incident polarization state, and the emergent Stokes vector is only determined by R3 and R4. This process can be visualized in the Poincare sphere which is $\hat{s}$ vector space, as shown in Figure 2. The transformation characterized by R3 is a rotation of $\hat{s}_{in}$ ($[0,\ 0,\ 1]^T$) by the angle δ_L along S_2-S_3, followed by a rotation of 2φ with respect to the S_3 axis characterized by R4. The angle between $\hat{s}_{in}$ and $\hat{s}_{out}$ is the magnitude of linear retardance δ_L. The linear retardance essentially serves as a mechanism to rotate $\hat{s}_{in}$ away from the S_3 axis.

Here, it is necessary to assume that the linear polarized components of the emergent light from tissue arise from the linear retardance of tissue. The magnitude of linear retardance can therefore be approximated by calculation of the angle between the incident polarization state vector [S_{in1}, S_{in2}, S_{in3}] denoted by $\hat{s}_{in}$ (which is [0, 0, 1] for circularly polarized light), and the emergent polarization state vector [S_{out1}, S_{out2}, S_{out3}] represented by $\hat{s}_{out}$.

$$\delta_{L\text{-}S} = \cos^{-1}\left(\frac{\hat{s}_{in} \bullet \hat{s}_{out}}{|\hat{s}_{in}||\hat{s}_{out}|}\right) \tag{4}$$

The magnitude of linear retardance $\delta_{L\text{-}S}$ (range 0° to 180°) is referred to as Stokes-retardance in this paper.

2.2.2 Interpretation from Mueller matrices

Mueller polarimetric images were analysed according to the widely used polar decomposition method proposed by Lu-Chipman [1, 19].

$$M = M_\Delta M_R M_D \tag{5}$$

where M_Δ, M_R, M_D are depolarization, retardance and diattenuation matrices respectively decomposed from a Mueller matrix M. These three matrices can be further interpreted into several physically meaningful quantities including depolarization powers, magnitudes of linear and circular retardance, linear retardance orientation (fast axis orientation), and magnitudes of linear and circular diattenuation. In order to compare with Stokes polarimetry method, only the magnitude of circular depolarization and linear retardance were assessed. We followed the convention in a number of references [2, 53-55] to calculate circular depolarization,

$$dep_{c\text{-}M} = 1 - |M_{\Delta(4,4)}| \tag{6}$$

$M_{\Delta(4,4)}$ is the bottom right element in the depolarization matrix. The circular depolarization power $dep_{c\text{-}M}$ obtained here is unitless and ranges from 0 (non-depolarized) to 1 (fully depolarized) with The linear retardance magnitude (range 0° to 180°) was reconstructed from the retardance matrix M_R according to [1, 2] as displayed in the following equation,

$$\delta_{L\text{-}M} = \cos^{-1}\left(\sqrt{(M_{R(2,2)} + M_{R(3,3)})^2 + (M_{R(3,2)} - M_{R(2,3)})^2} - 1\right) \tag{7}$$

The circular depolarization power $dep_{c\text{-}M}$ and linear retardance magnitude $\delta_{L\text{-}M}$ obtained from Lu-Chipman decomposition of a complete Mueller matrix here are referred to as Mueller-depolarization and Mueller-retardance respectively in this paper.

2.3 Image feature detection and matching

The scale-invariant feature transform, known as SIFT [56], was used to investigate image content similarity between circular-depolarization/linear-retardance images reconstructed from Mueller polarimetry and from Stokes polarimetry. SIFT is a widely-adopted algorithm in computer vision,

and mainly consists of three key steps: feature detection to find local image features, feature description to generate descriptors to describe those features, and feature matching to search for the correspondences between features from paired images. In feature detection, difference of Gaussians is firstly computed in scale space to a series of smoothed and resampled images, and the local extrema are found and treated as candidate features. This is then followed by a pruning procedure to eliminate low-contrast features and edge features, leaving only the effective ones. The magnitude and orientations of gradients are then calculated for all the effective features, and used to construct feature descriptors (128-element vectors). In feature matching, the Brute-Force Matching method is used to find feature pairs in paired images, by comparing feature descriptors. The feature pair with the smallest Euclidean distance is chosen as a matched feature (pair). Generally speaking, SIFT is scale- and rotation-invariant, and illumination-invariant to some extent, leading to robustness in finding matches in between paired images according to texture information. As is noticed that the circular-depolarization/linear-retardance images from Mueller polarimetry and Stokes polarimetry are generally similar in texture while slightly different in pixel values, SIFT is a suitable tool to evaluate the similarity between them. In our experiments, the algorithm was implemented using OpenCV on a GPU [57] for feature detection and matching between the images. Since a Mueller image and its corresponding Stokes image always share the same field-of-view, correctness of matches could be easily determined: correct matches are at the same locations, while the incorrect ones are not. The "feature matching rate" was defined as the number of correctly matched features divided by the total number of features detected (including those correctly and incorrectly matched). A high feature matching rate signifies good image content similarity.

3. Results and discussion

3.1 A case study using Setup 1: Porcine liver

Ex vivo porcine liver tissue was harvested from a Large White pig post mortem. The liver (thickness, maximum length and width are approximately 1 mm, 25 mm and 25 mm respectively) was dissected and held between two glass slides as illustrated by the photo in Figure 3(a). The central circular region with a diameter 18 mm was illuminated and imaged by Setup 1. The same piece of porcine liver tissue was imaged by Setup 1 in the transmission and reflection geometry. The elemental images in the first row and column of 4×4 Mueller matrix images M11 correspond to polarization insensitive images [58], and are shown in Figure 3(b) and (c) for reflected and transmitted geometry respectively. It is noted that the field-of-view and magnification of the imaging polarimeter in transmission and reflection geometry were not the same (see scale bars in Figure 3(b, c)). The Mueller matrix images were then divided by M11 pixel-wise to generate a normalised Mueller matrix (Figure 3(d, f)), where the elements corresponding to tissue diattenuation and polarizance – namely, M12, M13, M14, M21, M31, and M41 – were approximately equal to zero and confirming that diattenuation of the liver is weak. The non-diagonal form of the bottom right 3×3 submatrix revealed that the liver is essentially a depolarizing retarder. Hepatic lobules, the functional units of the liver that are normally approximately hexagonal, can be observed in the bottom right 3×3 submatrix images due to strong birefringence arising from the connective tissue at the border regions of each lobule. The Stokes polarimetric images of the liver in both geometries are shown in Figure 3(e, g). Birefringent hepatic lobule borders can be easily identified from S_1 and S_2 elemental images.
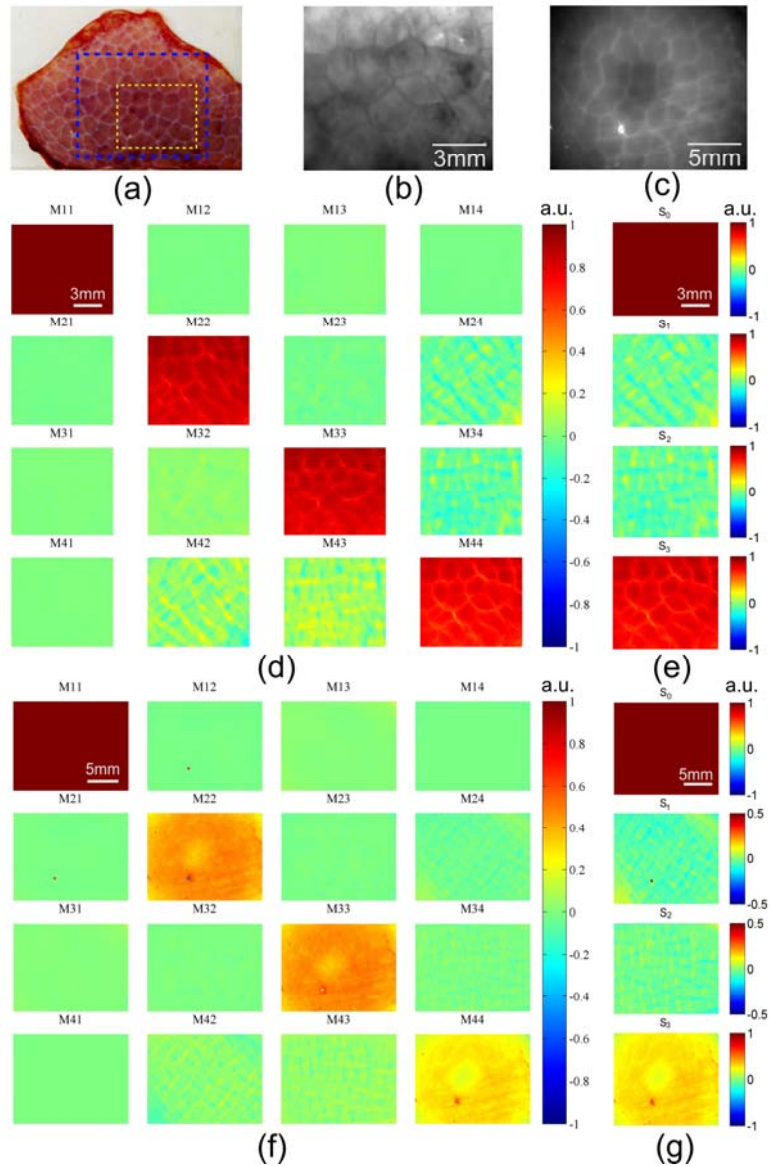
Figure 3 (a) Photograph of the liver sample; (b, c) polarization insensitive image of the liver sample obtained in transmission and reflection geometry respectively. The pixel values in (b,c) are dimensionless; (d, e) Mueller and Stokes polarimetric images in transmission geometry; (f, g) Mueller and Stokes polarimetric images in reflection geometry. The yellow and blue boxes in (a) correspond to the field of view of the images acquired in transmission and reflection geometry respectively. All the Mueller matrix element images in (d) share the same colour bar which is at the right of (d). The same applies to (f). All the elements in Mueller matrices and Stokes vectors are dimensionless quantities with arbitrary unit (a.u.).

For further analysis, these Mueller and Stokes polarimetric images were interpreted into tissue retardance and circular depolarization using Matlab® 2011 and a PC with 16G RAM and Intel® Core™ i5-3320M CPU 2.6GHz. Decomposition of Mueller matrices involves multiple matrix operations and eigenvalue calculations and has to be conducted pixel by pixel, resulting in long reconstruction time (two minutes). It took as little as 0.04 seconds to interpret Stokes polarimetric images, which only requires the most basic image-wise operations (image data are regarded as numeric arrays), namely, addition, multiplication, division, square and root square, as stated in Section 2.2, rather than pixel by pixel operations as required by Mueller matrix decomposition.

The interpretation time is one of the advantages of the Stokes method and make it more suitable for real-time polarimetric assessment.
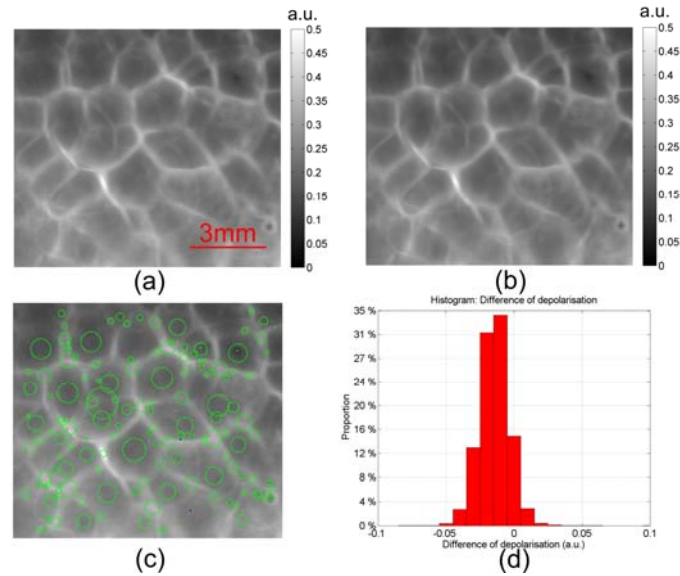

Figure 4 (a) Mueller-depolarization image acquired in transmission geometry. (b) Stokes-depolarization image acquired in transmission geometry. Mueller-depolarization and Stokes-value are dimensionless quantities with arbitrary unit (a.u.). (c) Correctly matched (green) and incorrectly matched (blue) features marked by circles on the Mueller depolarization image where the size of the circle represents the size of the feature. (d) The intensity histogram of the "difference image" obtained by subtracting the Stokes-depolarization image pixel-wise from the Mueller-depolarization image.

A tissue circular depolarization image obtained from Mueller matrices (referred to as Mueller-depolarization) is shown in Figure 4(a). It can be observed that depolarization in the central region of each hepatic lobule is lower than its borders, which may be caused by the lower birefringence of central lobules compared with the connective tissue at the borders. Birefringence in turbid media is known as a source of depolarization resulting from phase randomization during scattering. Lower absorption for the connective tissue compared with that of the central lobules is observable in the photograph of the liver sample in Figure 3(a), and normally results in the emergent light being more multiply-scattered and therefore more depolarized. Figure 4(b) shows a tissue circular depolarization image reconstructed from Stokes vectors (referred to as Stokes-depolarization). The Mueller-depolarization and Stokes-depolarization images demonstrate a highly similar pattern. SIFT was used to assess the similarity whereby features were first detected in the Mueller-depolarization image and then were matched with those from the Stokes depolarization image. Image similarity was then assessed by the percentage of features correctly matched. In total 194 features were detected in the Mueller-depolarization image and are marked by circles overlaid onto the Mueller-depolarization in Figure 4(c). The diameter of the circles represents the size of the detected feature. The correctly matched features are marked by green circles in the Mueller-depolarization image in Figure 4(c) for clarity, while the incorrect matches are marked by blue circles. The 98.97% feature matching rate illustrates that Mueller depolarization and Stokes depolarization images present highly similar information content. The diameters of all the features range from 4 pixels to 120 pixels for this set of results. The diameters of the two incorrectly matched features are 4 and 5 pixels respectively.

The difference between the Mueller-depolarization and Stokes-depolarization images was also quantitatively investigated by constructing a "difference image" through pixel-wise subtraction between the Stokes-depolarization and Mueller-depolarization images. The mean difference across the "difference image" is -0.0114/pixel and the root-mean-square(RMS) difference is 0.0181/pixel,

indicating that in general the Stokes method slightly undervalues the circular depolarization compared with the Mueller method. For the vast majority of pixels (95%), the absolute difference is less than 0.04. The quantitative difference between Stokes- and Mueller-depolarization is small, given that the range of the depolarization values in the raw images is from 0 to 1.
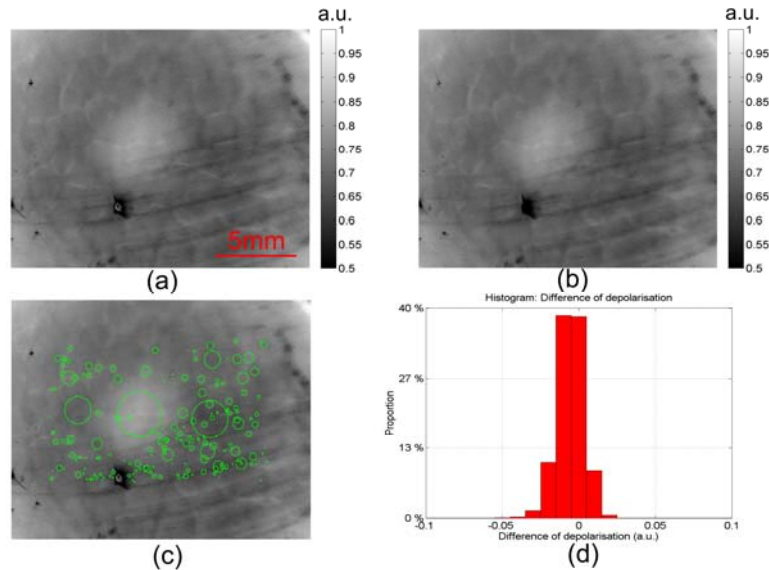

Figure 5 (a) Mueller-depolarization image acquired in reflection geometry. (b) Stokes-depolarization image acquired in reflection geometry. Mueller-depolarization and Stokes-value are dimensionless quantities with arbitrary unit (a.u.). (c) Correctly matched (green) and incorrectly matched (blue) features marked by circles on the Mueller-depolarization image where the size of the circle represents the size of the feature. (d) The intensity histogram of the "difference image" obtained by subtracting the Stokes-depolarization image pixel-wise from the Mueller-depolarization image.

In the reflection geometry (Figure 5), although the hepatic lobule structures in the depolarization image were generally not as clear as in the transmission geometry, depolarization of the connective tissue remains higher than for central lobules. Overall, the depolarization power of the liver tissue in reflection geometry was higher than that in transmission geometry. This was reasonable since the low order scattered light which underwent no or a limited number of scattering events was dominant in the transmitted light, considering the thickness of the tissue was about 1 mm. Low order scattered light is less depolarizing. In reflection geometry, the reflected light was however dominated by higher order scattered light, resulting in higher depolarization. It is noted that there is an artefact caused by the doughnut-shaped illumination (the illuminating light intensity in the central circular region is weaker than the surroundings). A portion of the light emergent from the central circular region was strongly depolarized as it consists of multiply-scattered photons that originate from the higher illumination intensity surrounding regions. This strongly depolarized portion could therefore apparently increase the depolarization of the central circular region. Given that illumination provided by the biomedical optical instruments like many microscopes and endoscopes are designed to be as homogeneous as possible [59], the artefacts are normally insignificant in practice. The same image feature matching methodology was applied to assess similarity of image content and quantitative difference between the Mueller-depolarization and Stokes-depolarization images shown in Figure 5(a) and (b). The edge of the field-of-view was not processed by SIFT due to insufficient illumination at the four corners resulting in poor signal-to-noise ratio that would affect SIFT. 220 features were detected in the Mueller-depolarization image and 100% of them were correctly matched with those in the Stokes depolarization image, as observed in Figure 5(c). The 100% matching rate suggested that information conveyed by these two images was equivalent. The mean intensity across the "difference image" constructed by image

subtraction was -0.0058/pixel and the RMS difference is 0.0181/pixel, which are similar to those for the transmission geometry. For the vast majority of pixels (94%), the absolute difference was less than 0.025. It can be summarized here that for the liver, the Mueller-depolarization and Stokes-depolarization image content acquired in both transmission and reflection geometries is highly similar, and the quantitative difference is small.

Due to birefringence arising from the connective tissue at the border regions of each lobule, the boundaries of the lobules demonstrate a higher linear retardance value than the central region. This can be observed from the linear retardance image in Figure 6(a) and (b) obtained from Mueller polarimetry (referred to as Mueller-retardance) and from Stokes polarimetry (Stokes-retardance) respectively in the transmission geometry. Figure 6(a) and (b) appear almost identical. The same feature matching comparison methodology was applied as for depolarization. Among 685 features detected in the Mueller-retardance image, 678 (98.98%) were matched with those in the Stokes-retardance image (Figure 6(c)). The diameters of the features mainly range from 4 pixels to 78 pixels for this set of results. All the incorrectly matched features were small local features (feature diameter 5-10 pixels) and are difficult to identify by eye in Figure 6(c). The mean and RMS difference in linear retardance value across the image (Figure 6(d)) was then calculated as 0.044°/pixel and 1.310°/pixel respectively. The difference for 56% of pixels is in the range of -1°~1°. The quantitative difference between Stokes- and Mueller-retardance is small, given that the range of the retardance values in the raw images is from 0° to 180°.
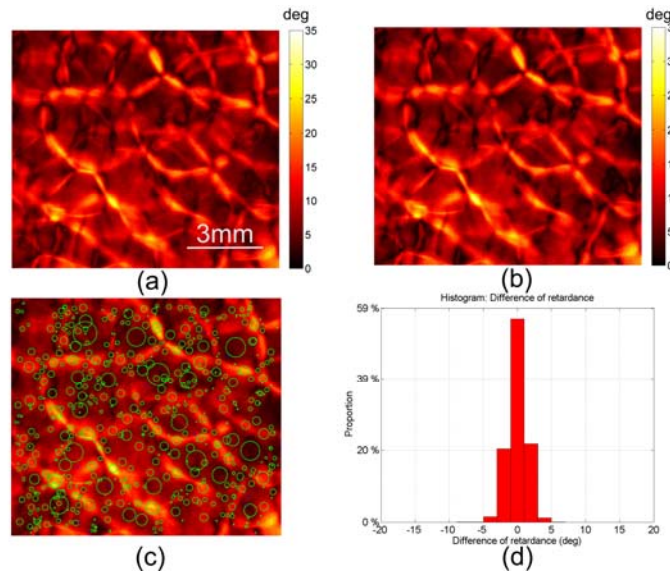

Figure 6 (a) Mueller-retardance image acquired in transmission geometry. (b) Stokes-retardance image acquired in transmission geometry. The unit of the colour bars is degrees (deg). (c) Correctly matched (green) and incorrectly matched (blue) features marked by circles on the Mueller-retardance image where the size of the circle represents the size of the feature. (d) The intensity histogram of the "difference image" obtained by subtracting the Stokes-retardance image pixel-wise from the Mueller-retardance image.

In the reflection geometry, although there are observable differences when comparing the Mueller-retardance and Stokes-retardance images in Figure 7(a) and (b), the pattern is qualitatively similar, showing the clear polygonal patterns as a result of birefringent connective tissue around the lobules. It is found by using SIFT that 85.53% of the total 325 features that were detected in the Mueller-retardance image were matched with those in the Stokes-retardance image, as shown in Figure 7(c). Incorrectly matched features (blue circles) were mainly distributed around three individual lobule borders indicated by the white arrows in Figure 7(c) because the contrast of the lobule borders was not sufficiently strong in the Stokes-retardance image. The diameters of the

features for this set of results range from 10 pixels to 85 pixels. The matching rate of the small size features is lower for that of the large ones in general. The matching rates of features in the range of 10-20 pixels, 20-30 pixels, and 30-40 pixels are 79.80%, 90.24%, and 91.43% respectively. For those with feature diameter larger than 40 pixels the matching rate is 100%. The mean value of the "difference image" between the Stokes-retardance and Mueller-retardance images over the entire field of view was 3.488°/pixel, and the RMS difference is calculated to be 6.266°/pixel. The intensity histogram of the "difference image" shown in Figure 7(d) indicates that the difference of 60% pixels is in the range of -5~5°. Mueller-retardance and Stokes-retardance images from a reflection geometry are qualitatively equivalent.
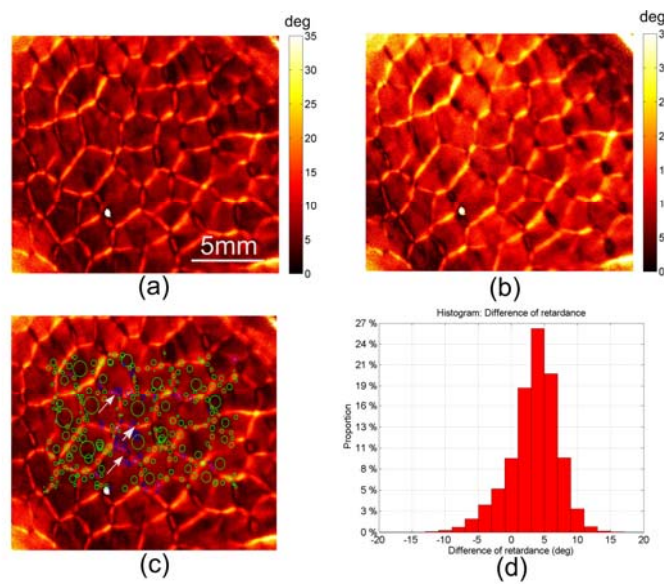

Figure 7 (a) Mueller-retardance image acquired in reflection geometry. (b) Stokes-retardance image acquired in reflection geometry. The unit of the colour bars is degrees (deg). (c) Correctly matched (green) and incorrectly matched (blue) features marked by circles on the Mueller retardance image where the size of the circle represents the size of the feature. (d) The intensity histogram of the "difference image" obtained by subtracting the Stokes-retardance image pixel-wise from the Mueller-retardance image.

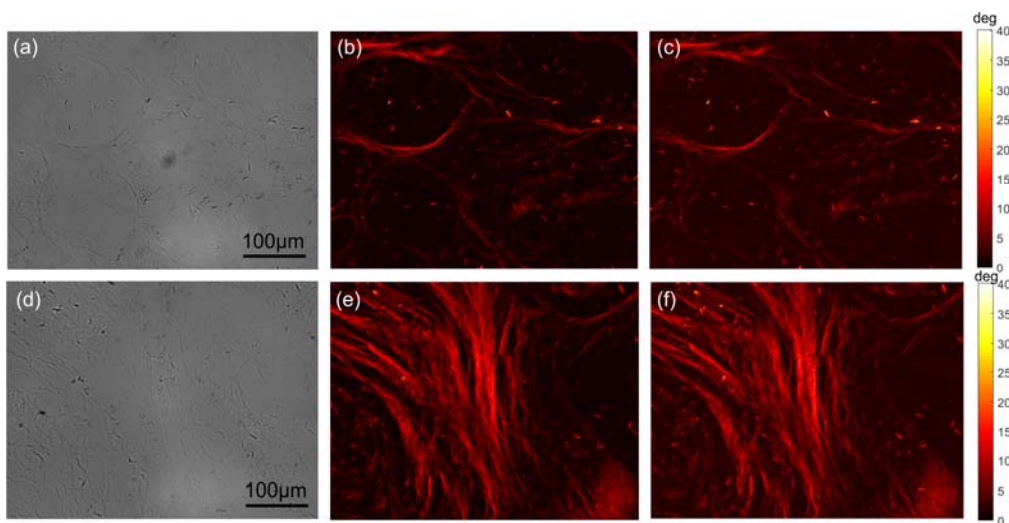### 3.2 A case study using Setup 2: unstained human breast microscope slides

Figure 8 The polarization insensitive images, Mueller-retardance and Stokes-retardance images of the unstained healthy breast tissue slide (a-c) and carcinoma in situ breast tissue slide (d-f). (b) and (c) share the same colour bar displayed at the right of (c). (e) and (f) share the same colour bar displayed at the right of (f). The unit of the colour bars is degrees (deg).

Two 12 μm thick unstained dewaxed human breast slides-one with ductal carcinoma tissue (referred to as cancerous) and one from healthy breast (referred to as healthy) - provided by Shenzhen Sixth People's (Nanshan) Hospital were imaged using Setup 2 which is a Mueller polarimetric transmission microscope. This work was approved by the Ethics Committee of the Shenzhen Sixth People's (Nanshan) Hospital. The polarization insensitive images of the two samples were displayed in Figure 8(a) and (d). It is impossible to observe any useful contrast to distinguish the two samples from the polarization insensitive images. The cancerous breast demonstrated a higher proportion of fibrous structures in and around the breast catheters resulting from breast fibrosis. Thus, it was observable that the cancerous sample contained more retarding tissue structures as shown in the Mueller-retardance image of the cancerous sample (Figure8(e)) than those in the health sample (Figure 8(b)) without the use of exogenous contrast agents. Stokes-retardance and Mueller-retardance images of both the samples look highly similar, as shown in Figure 8 (b VS c, e VS f). Using the Stokes polarimetry based method, it is also possible to differentiate the healthy and cancerous sample. The same feature matching comparison methodology was applied here. Among 669 features detected in the Mueller-retardance image of the healthy sample, 626 (93.58%) were correctly matched with those in the Stokes-retardance image (Figure 8(b) and (c)), and 914 out of 996 features (92.71%) detected in the Mueller-retardance image of the cancerous sample were correctly matched with those in the Stokes-retardance image (Figure 8(e) and (f)). The incorrectly matched features were mainly small local features and are difficult to identify by eye. The mean and RMS difference in linear retardance value, was then calculated as 0.196°/pixel and 1.386°/pixel between Figure 8(b)&(c), and 0.210°/pixel and 1.564°/pixel between Figure 8(e)&(f) respectively. Mueller-depolarization and Stokes-depolarization of both slides are not prominent, because these thin samples were weakly scattered. In this case, the proposed Stokes polarimetry with circularly polarized illumination and the Mueller polarimetry demonstrated nearly equivalent results. The results suggested that both Mueller and Stokes polarimetric microscopes could potentially offer a way to accelerate histopathology for breast ductal carcinoma by avoiding staining process.

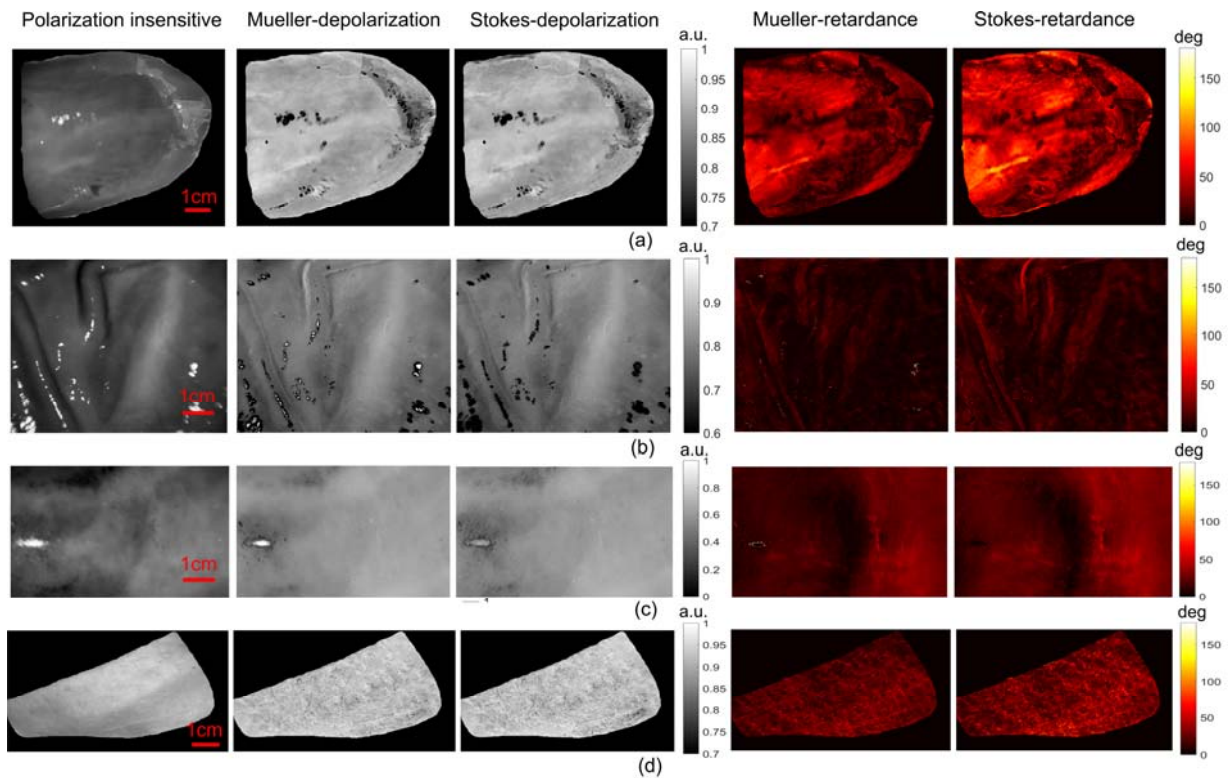**3.3 Case study using Setup 3: other bulk tissues**

Figure 9 The polarization insensitive, Mueller-depolarization, Stokes-depolarization, Mueller-retardance, Stokes-retardance images of (a) tongue, (b) stomach, (c) kidney and (d) belly. The second and third images in each row have the same colour bar displayed at the right of the third images. The fourth and fifth images in each row have the same colour bar displayed at the right of the fifth images. The unit of the colour bars for retardance images is degrees(deg).

A broader range of cases were studied using Setup 3 (reflection geometry). *Ex vivo* porcine tongue (bottom side), stomach (serosa side), kidney (kidney surface) and belly (skin side) tissues harvested from a Large White pig post mortem were imaged by Setup 3. It is noted that the samples were bulk tissues and only reflection geometry studies were conducted. As shown in the second and third columns of Figure 9, Mueller-depolarization and Stokes-depolarization images looked nearly the same intuitively for all the cases. By applying the feature matching comparison methodology, the matching rates for the tongue, stomach, kidney and belly were calculated as 89.01%, 87.71%, 91.96% and 87.59% respectively. The matching rate was high but lower than the liver sample shown in Figure 5. One of the reasons could be that some regions suffering from pixel saturation due to specular highlight on the tissue surface demonstrated different Mueller-depolarization and Stokes-depolarization features/values, as can be found in Figure 9 (b) and (c). The mean and RMS difference were also calculated as, 0.0007/pixel and 0.037/pixel for the tongue, 0.0001/pixel and 0.036/pixel for the stomach, 0.0002/pixel and 0.028/pixel for the kidney, 0.0013/pixel and 0.012/pixel for the belly. It came to the same conclusion as the liver experiment that Mueller-depolarization and Stokes-depolarization image content acquired in both reflection geometries is highly similar, and the quantitative difference is small. The Mueller-retardance and Stokes-retardance images were displayed in the fourth and fifth column of Figure 9 respectively. Their image contents were similar. Most of features in the Mueller-retardance images can be observed in the corresponding Stokes-retardance images, although there are also observable differences. The matching rates for the tongue, stomach, kidney and belly were calculated as 82.42%, 84.07%, 77.28% and 84.30% respectively. The mean and RMS difference were also calculated as, 8.6555°/pixel and 13.73°/pixel for the tongue, 2.8902°/pixel and 7.279°/pixel for the

stomach, 4.4417°/pixel and 6.520°/pixel for the kidney, 3.2891°/pixel and 9.639°/pixel for the belly. In accordance to the liver experiment, for reflection geometry detection, the Mueller-retardance images and Stokes-retardance images were qualitatively rather than quantitively the same. Most of the image contrast features in the Mueller-retardance images can be found in the corresponding Stokes-retardance images.

3.4 Case study using data generated from polarization sensitive Monte Carlo simulation

Polarimetric data generated from polarization sensitive Monte Carlo simulation were also used in this work. The simulation is based on the sphere birefringence model presented in [60, 61]. Birefringent tissues are simplified into turbid media with spherical microparticles as the main scatterer and a birefringent interstitial media. 0.2 μm diameter microspheres were chosen in accordance with our previous work [60, 61], and the thickness of the sample was set as 1 mm and the scattering coefficient was set at 30 cm^{-1}. The tissue birefringence was varied over 21 birefringence values with Δn ranging from 0 to 0.001, and the optic axis is parallel to the imaging plane, along 0° direction. Mueller matrices of the media with different birefringence values were then obtained and analyzed by polar decomposition methods. For the simulation of Stokes imaging, the emergent Stokes vectors were generated from the multiplication product of the obtained Mueller matrices and the Stokes vector of incident circularly polarized light represented by [1 0 0 1]. The output Stokes vectors were then analyzed using the method mentioned in Section 2. Both transmission and reflection geometry have been simulated with results presented in Fig. 10.

Generally, depolarization increases with tissue birefringence in the transmission mode as well as the reflection mode, as demonstrated in Figure 10(a, b), due to the rise of birefringence induced depolarization. The Mueller-depolarization and Stokes-depolarization curves are highly consistent for both geometries, matching tissue experiment observations. The average difference is as small as 1.781×10^{-3} for the transmission geometry and 0.0188 for the reflection geometry. In Figure 10(c), the retardance values vary periodically from 0° to 180° as the birefringence increases in the transmission geometry, similar to what would happen for transmissive optics. The average difference between Mueller-retardance and Stokes-retardance in the transmission geometry is only 0.6643° and the results from the two methods are highly similar in terms of the retardance value and the curve shapes. In the reflection geometry, the retardance values increase monotonically in the simulated birefringence range, as shown in Figure 10(d). When no birefringence was demonstrated in the media, Stokes-retardance and Mueller-retardance were both approximately zero, as expected. The two retardance curves still retained a similar shape and trend as the birefringence increases, and therefore the majority of image contrast information in a Mueller-retardance image arising from different birefringent properties of tissue would be preserved by Stokes polarimetric imaging. It is observed that the difference becomes larger as the birefringence of the medium increases. The mean difference between Stokes-retardance and Mueller-retardance in the reflection geometry is 18.4°. Overall, the retardance values obtained from these two methods are qualitatively rather than quantitatively the same in reflection geometry. Stokes-retardance is able to maintain the same form of line profile, which suggests that the majority of useful image contrast would be preserved in general by Stokes retardance images.
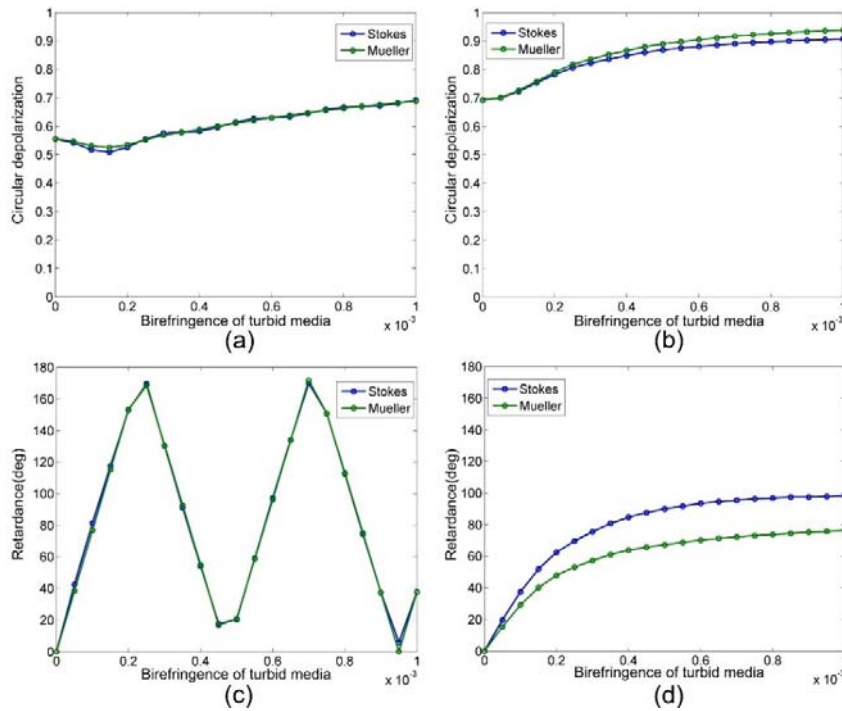
Fig. 10 Monte Carlo simulation of turbid media with depolarization and retardance. Green and blue curves were obtained from Mueller polarimetry and Stokes polarimetry respectively. Depolarization curves in (a) transmission and (b) reflection geometries. Retardance curves in (c) transmission and (d) reflection geometries.

4. Summary

In tissue Mueller polarimetry, it is popular to extract the physically meaningful information (depolarization, retardance, etc.) via Mueller matrix decomposition, and then to correlate with clinical information. The Mueller matrix decomposition serves as a helpful research tool to facilitate investigation and understanding of biophysical origin of the polarimetric signals and as a useful method to obtain azimuthal orientation angle independent polarization property parameters to maintain the reproducibility of results [25]. In this study, the circular polarized illumination was used to achieve azimuthal orientation angle independence, and a Stokes polarimetric measurement of emergent light from the tissue was used to approximate two of the main polarization properties.

In this study tissue circular depolarization and linear retardance obtained from Stokes polarimetry have been compared with those from the more complete Mueller polarimetry both in transmission and reflection geometries. Based on the experimental work on several porcine tissues and human breast slides and the data generated by simulation, we found that circular depolarization obtained using these two methods is very close for both transmission and reflection geometries, and that linear retardance is quantitatively similar for the transmission geometry and qualitatively for the reflection geometry. Most tissue circular depolarization and linear retardance image information (represented by local image contrast features) obtained from Mueller polarimetry is well preserved for Stokes polarimetry in both geometries. The difference between Mueller-depolarization and Stokes-depolarization is not significant to strongly affect quantitative data analysis. The difference between Stokes- and Mueller- retardance is however pronounced for reflection geometry. Stokes-retardance obtained in reflection geometry is generally not precise enough for further data processing to derive other quantitative parameters, for example, using retardance information obtained from Stokes polarimetry in reflection geometry to derive tissue

birefringence values, etc. In practice, it should be considered case by case whether the difference between Stokes- and Mueller- retardance is acceptable or not for a specific application.

It is also noted that there are also other perspectives to extract useful information measured by tissue Stokes polarimetry e.g. [33], but the Stokes method proposed here has the advantage that many findings and application of tissue Mueller polarimetry can be referred to for understanding tissue Stokes polarimetric data. Stokes polarimetry, as a passive polarimetric technique, can be implemented using much simpler instrumentation, and Stokes polarimetric images can be acquired and analysed faster. Furthermore, this approach allows further application of Stokes polarimetry where Mueller polarimetric imaging is difficult to implement, such as for polarimetric endoscopy. This study also suggests that where short acquisition times, instant polarimetric image analysis or low optical system complexity are priorities, Stokes polarimetry could become a useful method to assess circular depolarization and to approximate linear retardance for many anisotropic tissues with weak diattenuation.

Acknowledgement

References

[1] S.-Y. Lu, R. A. Chipman *J. Opt. Soc. Am. A*. 13, 1106-1113 (**1996**).
[2] N. Ghosh, I. A. Vitkin, M. F. G. Wood *J. Biomed. Opt.* 13, 044036-044036 (**2008**).
[3] J. Qi, D. S. Elson *Sci Rep*. 6, 25953 (**2016**).
[4] J. Qi, C. Barrière, T. C. Wood, D. S. Elson *Biomed. Opt. Express*. 3, 2087-2099 (**2012**).
[5] J. Qi, M. Ye, M. Singh, N. T. Clancy, D. S. Elson *Biomed. Opt. Express*. 4, 2433-2449 (**2013**).
[6] S. Forward, A. Gribble, S. Alali, A. A. Lindenmaier, I. A. Vitkin *Scientific Reports*. 7, 11958 (**2017**).
[7] S. Alali, K. J. Aitken, A. Schröder, A. Gribble, D. J. Bagli, I. A. Vitkin *Biomed. Opt. Express*. 5, 621-629 (**2014**).
[8] E. Du, H. He, N. Zeng, M. Sun, Y. Guo, J. Wu, S. Liu, H. Ma *J. Biomed. Opt.* 19, 076013-076013 (**2014**).
[9] C. He, H. He, J. Chang, Y. Dong, S. Liu, N. Zeng, Y. He, H. Ma *Biomed. Opt. Express*. 6, 2934-2945 (**2015**).
[10] Y. Wang, H. He, J. Chang, C. He, S. Liu, M. Li, N. Zeng, J. Wu, H. Ma *J. Biomed. Opt.* 21, 071112-071112 (**2016**).
[11] I. Ahmad, A. Gribble, M. Ikram, M. Pop, A. Vitkin *J. Biophotonics*, n/a-n/a (**2015**).
[12] I. Ahmad, A. Gribble, I. Murtza, M. Ikram, M. Pop, A. Vitkin *PLOS ONE*. 12, e0175173 (**2017**).
[13] T. Novikova, A. Pierangelo, S. Manhas, A. Benali, P. Validire, B. Gayet, A. De Martino *Appl. Phys. Lett.* 102, 241103 (**2013**).
[14] A. Pierangelo, A. Benali, M.-R. Antonelli, T. Novikova, P. Validire, B. Gayet, A. De Martino *Opt. Express*. 19, 1582-1593 (**2011**).
[15] J. Wang, W. Zheng, K. Lin, Z. Huang *Biomed. Opt. Express*. 7, 1116-1126 (**2016**).
[16] A. Pierangelo, S. Manhas, A. Benali, C. Fallet, J.-L. Totobenazara, M.-R. Antonelli, T. Novikova, B. Gayet, A. De Martino, P. Validire *J. Biomed. Opt.* 18, 046014-046014 (**2013**).
[17] L. Qiu, D. K. Pleskow, R. Chuttani, E. Vitkin, J. Leyden, N. Ozden, S. Itani, L. Guo, A. Sacks, J. D. Goldsmith, M. D. Modell, E. B. Hanlon, I. Itzkan, L. T. Perelman *Nat Med*. 16, 603-606 (**2010**).
[18] K. Kanamori *J. Biomed. Opt.* 21, 071105-071105 (**2015**).
[19] J. Qi, H. He, H. Ma, D. S. Elson *Opt. Lett.* 42, 4048-4051 (**2017**).
[20] N. Ortega-Quijano, J. L. Arce-Diego *Opt. Lett.* 36, 1942-1944 (**2011**).
[21] R. Ossikovski *Opt. Lett.* 36, 2330-2332 (**2011**).

[22] N. Agarwal, J. Yoon, E. Garcia-Caurel, T. Novikova, J.-C. Vanel, A. Pierangelo, A. Bykov, A. Popov, I. Meglinski, R. Ossikovski *Opt. Lett.* 40, 5634-5637 (**2015**).
[23] H. He, N. Zeng, E. Du, Y. Guo, D. Li, R. Liao, H. Ma *Photonics & Lasers in Medicine*. 2, 129-137 (**2013**).
[24] M. Sun, H. He, N. Zeng, E. Du, Y. Guo, S. Liu, J. Wu, Y. He, H. Ma *Biomed. Opt. Express*. 5, 4223-4234 (**2014**).
[25] J. Qi, D. S. Elson *J. Biophotonics*, n/a-n/a (**2017**).
[26] J. Qi, C. He, D. S. Elson *Biomed. Opt. Express*. 8, 4933-4946 (**2017**).
[27] J. S. Tyo, D. L. Goldstein, D. B. Chenault, J. A. Shaw *Appl. Opt.* 45, 5453-5469 (**2006**).
[28] P.-Y. Deschamps, F.-M. Bréon, M. Leroy, A. Podaire, A. Bricaud, J.-C. Buriez, G. Seze *IEEE Transactions on geoscience and remote sensing*. 32, 598-615 (**1994**).
[29] F. Snik, J. Craven-Jones, M. Escuti, S. Fineschi, D. Harrington, A. De Martino, D. Mawet, J. Riedi, J. S. Tyo in An overview of polarimetric sensing techniques and technology with applications to different research fields, Vol., International Society for Optics and Photonics, City, pp.90990B-90990B-90920 (**2014**).
[30] P. J. Wu, J. J. T. Walsh *J. Biomed. Opt.* 11, 014031-014031-014010 (**2006**).
[31] P. J. Wu, J. T. Walsh *Lasers Surg. Med.* 37, 396-406 (**2005**).
[32] C. Macdonald, I. Meglinski *Laser Physics Letters*. 8, 324-328 (**2011**).
[33] B. Kunnen, C. Macdonald, A. Doronin, S. Jacques, M. Eccles, I. Meglinski *J. Biophotonics*. 8, 317-323 (**2015**).
[34] N. Ghosh, I. A. Vitkin *J. Biomed. Opt.* 16, 110801 (**2011**).
[35] A. Vitkin, N. Ghosh, A. d. Martino in *Tissue Polarimetry,* John Wiley & Sons, Inc., pp.239-321 (**2015**).
[36] N. Ghosh, M. F. Wood, I. A. Vitkin *Optics Communications*. 283, 1200-1208 (**2010**).
[37] R. M. A. Azzam *Opt. Lett.* 2, 148-150 (**1978**).
[38] E. Compain, S. Poirier, B. Drevillon *Appl. Opt.* 38, 3490-3502 (**1999**).
[39] R. Ossikovski, M. Anastasiadou, S. Ben Hatit, E. Garcia‐Caurel, A. De Martino *physica status solidi (a)*. 205, 720-727 (**2008**).
[40] R. Ossikovski *Opt. Lett.* 37, 220-222 (**2012**).
[41] J. J. Gil, E. Bernabeu *J. Mod. Opt.* 33, 185-189 (**1986**).
[42] R. A. Chipman *Appl. Opt.* 44, 2490-2495 (**2005**).
[43] S. R. Cloude, E. Pottier *IEEE Transactions on Geoscience and Remote Sensing*. 35, 68-78 (**1997**).
[44] R. Ossikovski, A. De Martino, S. Guyot *Opt. Lett.* 32, 689-691 (**2007**).
[45] R. Ossikovski *JOSA A*. 26, 1109-1118 (**2009**).
[46] V. Sankaran, M. J. Everett, D. J. Maitland, J. T. Walsh *Opt. Lett.* 24, 1044-1046 (**1999**).
[47] V. Sankaran, J. J. T. Walsh, D. J. Maitland *J. Biomed. Opt.* 7, 300-306 (**2002**).
[48] V. Backman, R. Gurjar, K. Badizadegan, I. Itzkan, R. R. Dasari, L. T. Perelman, M. S. Feld *IEEE J. Sel. Top. Quantum Electron*. 5, 1019-1026 (**1999**).
[49] R. S. Gurjar, V. Backman, L. T. Perelman, I. Georgakoudi, K. Badizadegan, I. Itzkan, R. R. Dasari, M. S. Feld *Nat Med*. 7, 1245-1248 (**2001**).
[50] S. L. Jacques, J. C. Ramella-Roman, K. Lee *J. Biomed. Opt.* 7, 329-340 (**2002**).
[51] R. A. Chipman in Polarization analysis of optical systems, Vol., International Society for Optics and Photonics, City, pp.10-31 (**1988**).
[52] S. Manhas, M. Swami, P. Buddhiwant, N. Ghosh, P. Gupta, K. Singh *Opt. Express*. 14, 190-202 (**2006**).
[53] N. Ghosh, M. F. Wood, I. A. Vitkin *J. Appl. Phys*. 105, 102023 (**2009**).
[54] M. Ahmad, S. Alali, A. Kim, M. F. G. Wood, M. Ikram, I. A. Vitkin *Biomed. Opt. Express*. 2, 3248-3258 (**2011**).
[55] S. Alali, M. Ahmad, A. Kim, N. Vurgun, M. F. G. Wood, I. A. Vitkin *J. Biomed. Opt*. 17, 045004-045001 (**2012**).
[56] D. G. Lowe *International Journal of Computer Vision*. 60, 91-110 (**2004**).
[57] OpenCV in Feature Matching, Vol., City).
[58] R. A. Chipman *Handbook of optics*. 2, 1-28 (**1995**).
[59] R. Liang, Optical design for biomedical imaging, Spie Press(**2010**).
[60] H. He, N. Zeng, R. Liao, T. Yun, W. Li, Y. He, H. Ma *Opt. Express*. 18, 15104-15112 (**2010**).
[61] H. He, N. Zeng, E. Du, Y. Guo, D. Li, R. Liao, Y. He, H. Ma *J. Biomed. Opt.* 18, 046002-046002 (**2013**).

Graphical Abstract

This study suggests that where short acquisition times, instant polarimetric image analysis or low optical system complexity are priorities, Stokes polarimetry could become a useful method to assess circular depolarization and to approximate linear retardance for many anisotropic tissues with weak diattenuation.

ToC figure